Journal of Superconductivity and Novel Magnetism (2021) 34:763–780
https://doi.org/10.1007/s10948-020-05754-1

ORIGINAL PAPER

Investigations on the Structural and Electrical Properties of Sm^{3+}-Doped Nickel Ferrite–Based Ceramics

Mehjabeen Khan[1] · Supriya Bisen[1] · Jyoti Shukla[1] · Ashutosh Mishra[1] · Pradeep Sharma[2]

Received: 1 September 2020 / Accepted: 4 November 2020 / Published online: 26 November 2020

Abstract

Compositions of ferrimagnetic $NiSm_xFe_{2-x}O_4$ ($0.00 \le x \le 0.25$) ceramics were synthesized by the self-propagating sol-gel autocombustion method. Structural information was found using X-ray diffraction. It reveals that all the ceramics possess cubic symmetry of spinel ferrite with a small amount of orthoferrite phase $SmFeO_3$, which is a ferroelectric material. The amount of phases and lattice parameter were determined by the Rietveld refinement method using the Fullprof suite software. As doping concentration increases, the secondary phase fraction of the ferroelectric $SmFeO_3$ also increases. Due to the increase of the ferroelectric phase in $NiFe_2O_4$, the electrical properties of doped samples also modify. To know this modification, the electrical properties of these samples have been investigated. The room temperature dielectric and complex impedance analysis have been measured in the frequency range of $1–10^6$ Hz. The dielectric behavior for $x = 0.05$ concentration ($NiSm_{0.05}Fe_{1.95}O_4$) has a maximum dielectric constant value with a minimal loss tangent. Cole-Cole plot brings out the role of grain and grain boundaries in the bulk. Using impedance study, the resistance and capacitance of grain and grain boundaries have been determined. The ferroelectric behavior has been performed through the *P-E* (polarization versus electric field) and *J-E* (leakage current versus electric field) curves at room temperature.

Keywords Ferrites · Sol-gel autocombustion · XRD · Dielectric behavior · Cole-Cole plot · Space charge limited conduction

1 Introduction

In the last decade, spinel ferrites have been extensively used as materials from a technological point of view because of their superior electrical, magnetic, and optical properties such as high saturation magnetization (M_s) as well as high dielectric properties [1]. Based on the available ferrites, nickel ferrite ($NiFe_2O_4$) is an essential magnetic material because of its chemical stability high electrical resistivity and low magnetic coercivity, which is primarily required in technological applications, such as in transformer cores, microwave devices, and magnetic storage devices in electronics and telecommunication, targeted drug delivery agents in medicine, and lithium-ion batteries and nanocatalysis agents in the energy industry [2].

✉ Mehjabeen Khan
mehjabeen.khan2013@gmail.com

[1] School of Physics, Devi Ahilya University, Khandwa Road Campus, Indore 452001, India

[2] Govt. Holkar Science College, Indore 452001, India

The spinel ferrites adopt one of the three kinds of structure: inverse, normal, or mixed cubic spinel structure. Nickel ferrite adapted an inverse spinel crystal structure. In this crystalline structure, anions (oxygen) form face-centered cubic arrangements, and metal cations $8Ni^{2+}$ ions are distributed at octahedral (O_d) sites while $16Fe^{3+}$ occupied equally the tetrahedral (T_d) and octahedral (O_d) sites [3]. There are various techniques for the synthesis approach used to fabricate the nickel ferrite such as co-precipitation, microwave synthesis, thermal decomposition, sol-gel autocombustion method, citrate-nitrate–assisted, electrospinning, reverse micelle, and ultrasonication [4]. One of the abovementioned techniques, the sol-gel autocombustion approach has proved to be a time-saving method for easily obtaining high-purity materials. When compared with other traditional methods, this approach provides low-cost and simple tools, the formation of desired products at low temperature, and easy-to-control particle size and stoichiometry [5].

Many researchers tried to enhance the structural and magnetic properties of $NiFe_2O_4$ by substituting varieties of magnetic, nonmagnetic, and rare earth ions active metals. One of the highly promising alternatives to enhance the features of

spinel ferrites is the rare earth (RE) ions [6]. As far as the magnetic moment of rare earth ions is concerned, it ranges from 0 (La^{3+}) to 10.5 μ_B (Dy_{3+}) that makes them able to demonstrate a variety of magnetic variations [7]. Due to the existence of multiplicity in both ground and first excited spins states, which are highly degenerate, the rare earth isolated Sm^{3+} ions exhibit interesting magnetic moment. The experimentally observed magnetic moment (0.84 μ_B) has a major mismatch with the theoretical (1.74 μ_B) values that are generally referred to as the Van Vleck effect [8]. Modified magnetic properties of Samarium (Sm^{3+})-doped nickel ferrites were analyzed through low-temperature magnetization, zero-field cooled (ZFC), and field cooled (FC) measurements. Such samples have shown a super-paramagnetic (SPM) response with very low coercivity (H_c) and remanence magnetization (M_r), and this makes them ideal for the development of soft magnets [9]. The electrons in the 4*f* shell of the RE metals are the sources of magnetism, but they are shielded by shells of 5*s* 5*p*. The interaction between the rare earth ion and ferrite ion occurs through the 4*f*-3*d* coupling [2].

Earlier studies involve various complications in the synthesis of rare earth–doped ferrites in a single-phase rare earth–based ions with larger radii than Fe^{3+} tending to spread on grain boundaries of the spinel network even with very little content, causing the precipitation of crystalline or extra secondary phases of orthoferrite ($RFeO_3$), which strongly affects the transport, dielectric, and magnetic properties of the host material [7]. The composition of these types of secondary phase ($RFeO_3$) is orthorhombic unit cells with a distorted perovskite structure [10]. In such a structure, the iron atoms are slightly canted resulting in weak ferromagnetic interactions. Since the $RFeO_3$ compounds are included in the family of centrosymmetric ferrites, there still exists the ferroelectric property at room temperature where the non-equivalent spins are responsible for the induced ferroelectric property [11].

To the best of our knowledge, this is the first investigation that utilized ferroelectric, dielectric, transport, and leakage current behaviors to perform samarium-substituted nickel ferrite. This study aims to obtain $NiSm_xFe_{2-x}O_4$ ferrites using a self-propagating sol-gel autocombustion method and to investigate the structural and electrical properties of nickel ferrite–based ceramics. Besides, a complete description of the modulus and impedance study is performed to disclose the role of grain and grain boundaries to the mechanism of electrical transport and relaxation.

2 Experimental Details

2.1 Sample Preparation

Materials Required All the chemicals were used for this study without any further purification. For this goal, highly pure raw chemical materials iron(III) nitrate nonahydrate purified $Fe(NO_3)_3{\cdot}9H_2O$ [≥ 98% Merck], nickel(II) nitrate AR hexahydrate $Ni(NO_3)_2{\cdot}6H_2O$ [99% LOBA Chemie], samarium(III) nitrate hexahydrate $Sm(NO_3)_3{\cdot}6H_2O$ were prepared by samarium oxide AR Sm_2O_3 [99.9% LOBA Chemie], and nitric acid HNO_3, citric acid anhydrous $C_6H_8O_7$, ethylene glycol $C_2H_6O_2$, ammonia solution NH_4OH, polyvinyl alcohol $(C_2H_4O)_n$, and distilled water were selected.

Synthesis of Samarium Nitrate To ensure the production of samarium nitrate, the stoichiometric quantity of Sm_2O_3 was liquefying at 90 °C in a solution of nitric acid. The solution was then vaporized up to dryness, and the remaining content was dissolved in purified water to create a solvent for samarium nitrate. The feasible chemical reaction for the samarium nitrate hexahydrate synthesis can be illustrated through the following equation:

$$Sm_2O_3 + 6HNO_3 \rightarrow 2Sm(NO_3)_3 + 3H_2O$$

Synthesis of Sm-Doped Nickel Ferrite Different concentrations of rare earth samarium doped nickel ferrites, i.e., $NiSm_xFe_{2-x}O_4$ ($0.00 \le x \le 0.25$) were synthesized by self-propagating sol-gel autocombustion method. In this study, a combination of two fuels was used: (1) citric acid and (2) ethylene glycol. The citric acid was used as the complexing agent and ethylene glycol was used as the gelating reagent, which helps to form monophasic spinel ferrites. The fuel-to-nitrate ratio was calculated based on total oxidization and reduction of nitrate, fuel, and oxidizer valencies, respectively. The required ratio of precursors, the dopants, and both the fuels was measured individually using a digital balance (Shimadzu) and liquefied individually in a minimum amount of distilled water. These aqueous solutions are blended. The obtained solution was further stirred for 30 min at room temperature on a magnetic stirrer at 500 RPM until a homogenous mixture was obtained. The aqueous ammonia (NH_4OH) was added dropwise into the homogenous mixture to maintain pH 7 of the solution and to complete 3D networks. The well-stirred homogenous neutralized solution was then heated at a temperature of 90 °C on a magnetic stirrer to form a viscous gel. This viscous gel was further heated at 400 °C on a heating calotte to promote the self-ignition process. The self-ignition process capitulated a voluminous and fluffy product. The fluffy powder was grounded in agate mortar and pestle to get fine powders. The as-prepared powders were calcined in a furnace in an air atmosphere at 900 °C for 2 h for spinel phase formation. Furthermore, all the calcined powders were pressed into cylindrical pellets with a diameter of 10 mm and nearly 1 mm thickness by applying a pressure of 6 tons using a hydraulic press. These pellets were sintered at 1100 °C for 1 h to obtain a compact and less porous material. For dielectric measurement, the adjacent surfaces of pellets were coated with a thin layer of silver

paste for improved electrical communication. The flow chart of the synthesis procedure is given in Fig. 1. The prepared pallets were designated as Sm00, Sm05, Sm10, Sm15, Sm20, and Sm25, respectively, with increasing Sm content in $NiFe_2O_4$.

2.2 Sample Characterizations

To classify the phase formation and atomic arrangements of the sintered pellet, X-ray diffraction was recorded using the Bruker D8 Advance equipped with monochromatic CuKα source of radiation (λ = 1.5406 Å) with a current (18 mA) and a steady voltage (40 kV). The scan speed was 0.019°/s; the scan angle ranges from 10 to 90°. To know the phase fraction of the sintered samples, Rietveld refinement was done using the Fullprof software. The room temperature dielectric measurement and complex impedance analysis have been measured using the Broadband Dielectric Impedance analyzer (NovoControl) in the frequency range of 1–10^6 Hz. The radiant-precision material analyzer was used for the ferroelectric study at room temperature with each sample pressed, covered by or without silver electrodes on both sides.

3 Results and Discussions

3.1 Structural Study

X-ray diffraction patterns of the $NiFe_{2-x}Sm_xO_4$ (x = 0.0, 0.05, 0.10, 0.15, 0.20, and 0.25) ceramics are displayed in Fig. 2. All the XRD patterns validate that all the ceramics possessed a

Fig. 1 Flow chart of synthesis of $NiFe_{2-x}Sm_xO_4$ ceramics using self-propagating sol-gel autocombustion method

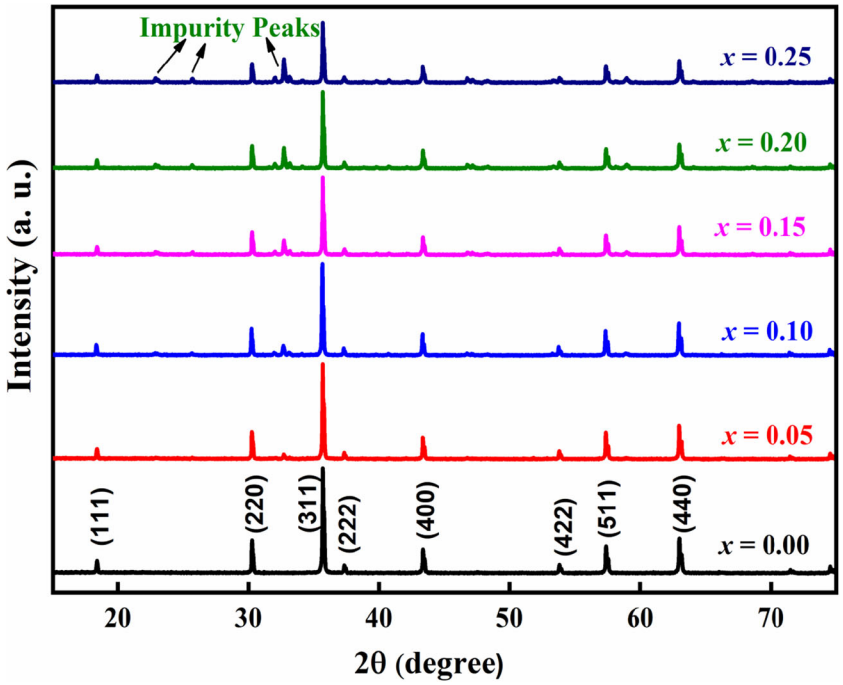

Fig. 2 X-ray diffraction patterns of $NiFe_{2-x}Sm_xO_4$ ceramics with different Sm content

polycrystalline cubic symmetry with inverse spinel structure and space group *Fd3m* (227), and the reflection planes (111), (220), (311), (222), (400), (422), (511), and (440) are perfectly indexed and well matched to the $NiFe_2O_4$ (JCPDS Card No. 100-325) [12–14]. Furthermore, we have noticed that samples exhibit a pure spinel phase only for $x = 0.0$ (without doping of samarium). When Sm^{3+} ions were doped in nickel ferrite, there is the emergence of few very weak peaks of the second phase that also appears with the spinel phase. The secondary phase corresponds to the $SmFeO_3$ phase which has an orthorhombic structure with space group *Pbnm*. The appearance of the second phase might be due to the isolation of Sm^{3+} ions at the grain boundary, indicating the solubility edge of Sm^{3+} at the spinel structure [15]. Due to their larger radii, Sm^{3+} ions are not accommodated in the spinel lattice and start to segregate at grain boundaries. With increasing the Sm^{3+} content, the intensity of the secondary phase also increases. It suggests that the Sm^{3+} did not generate a solid solution or had a very poor solid solubility with spinel ferrites. The ionic radius of Sm^{3+} ion is (0.958 Å) higher than that of Fe^{3+} (0.645 Å), and thus, there is a solubility limit for replacing Fe^{3+} ions with Sm^{3+} ions, and it is predicted that the excess substitution of Sm^{3+} ions appears to accumulate in the form of $SmFeO_3$ across the grain boundaries [16].

Figure 3 represents the Rietveld refinement analysis of dual-phase $NiFe_{2-x}Sm_xO_4$ ceramics sintered at 1100 °C. The refined XRD profile was obtained using the Fullprof software and analyzed by providing the required structural information from the literature. It indicates that the diffraction peaks belonging to the cubic spinel structure of $NiFe_2O_4$ and orthorhombic (with distorted perovskite) structure of $SmFeO_3$. It has been noticed that the amplitude of the ferroelectric $SmFeO_3$ peaks increases as the samarium content rises, and at the same time, the ferrite peaks decrease. The consistency of fit to the observed pattern of XRD was evaluated through the factors of the Rietveld agreement (R_p, R_{wp}, and χ^2). A good similarity was noted between the observed and calculated patterns of diffraction (Fig. 3) using the Rietveld analysis which is confirmed by observing the patterns of difference in measured and calculated XRD patterns. Table 1 shows the refined structural parameter values including crystallite size, lattice parameter, and unit cell volume of both phases of the samples. Phase fraction is also estimated from Rietveld refinement and also mentioned in Table 1. For pure nickel ferrite, the value of lattice constant, determined with the co-precipitation procedure is 8.3381 Å which is very close to that for the stated $NiFe_2O_4$ value [17]. With Sm^{3+} doping concentration, no regular trend has been noticed in the lattice parameter. The lattice parameter independence on Sm^{3+} concentrations clearly shows the quarantine of samarium in the boundaries of the grain. This could be demonstrated by the fact that nickel ferrite reveals the mixed existence of the spinel such that some of the Ni ions are transferred to the B-site. The presence of Sm ions at the B-site raises the strain, but the transfer of nickel ions from B-site to A-site decreases the strain to strengthen the structure; thus, the lattice parameter shows little variance with low Sm concentration. Sm originates to the grain boundaries for high concentration and does not act on the lattice parameter [18]. The X-ray density estimated for $NiFe_2O_4$ is 5.47 g/cm^3. With Sm^{3+} replacement, it has been found that the X-ray intensity increases. The increased value of the X-ray density can be described in such a manner that the samarium ion molar

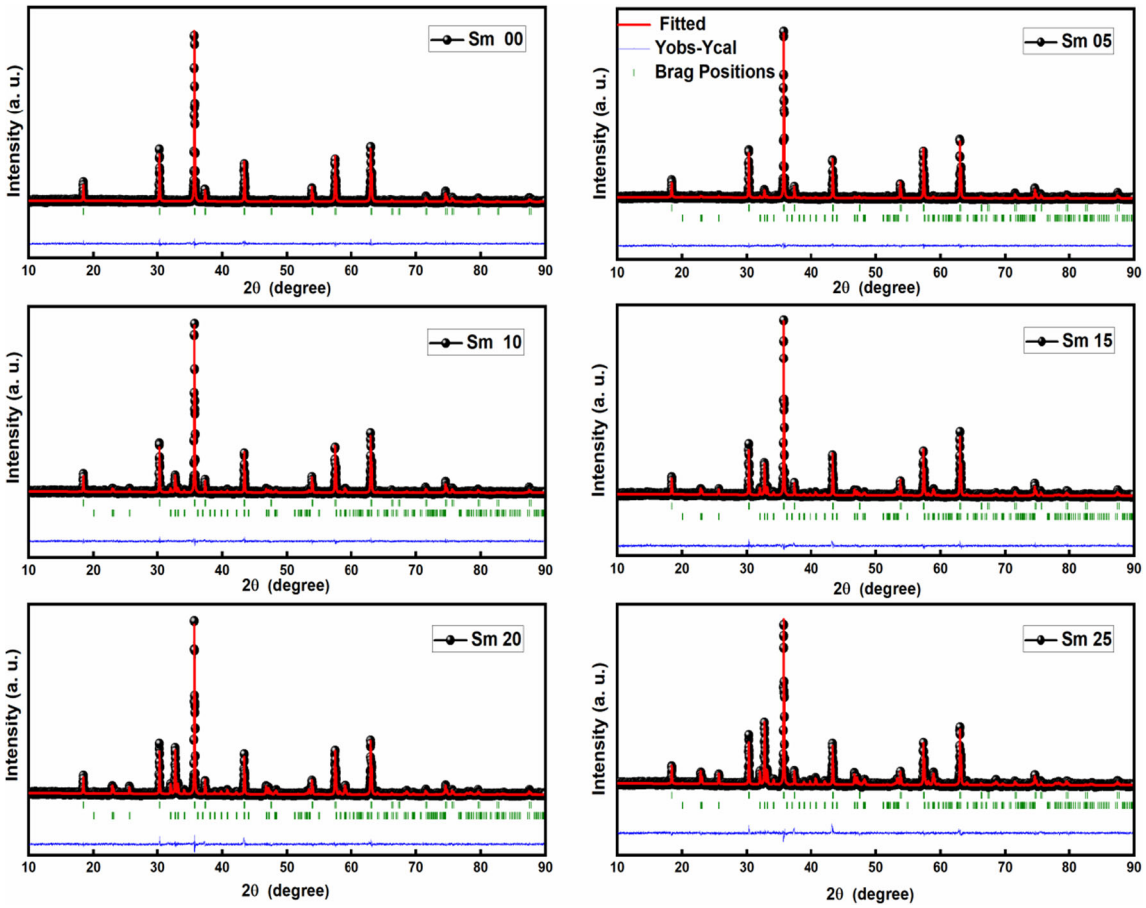

Fig. 3 Rietveld refinement plots of $NiFe_{2-x}Sm_xO_4$ ceramics with different Sm content

density is very large in contrast to iron ions. Due to the massive nature of samarium, the molecular weights of the samples have been increased with samarium concentration, and the X-ray density explicitly depends on the molecular mass and the lattice parameter [19]. The crystallite size of all the calcined powders was estimated from Sherrer's formula [20], and the average crystallite size (D) is also given in Table 1. The crystallite size increases with the doping of Sm^{3+}. This could be owing to the presence of the orthoferrite phase of $SmFeO_3$. When the doping amount of Sm^{3+} goes up, Sm^3 begins to reach the boundary of the grain, and the extra Sm at the grain boundary are responsible to develop the $SmFeO_3$ phase. This observation shows that part of the energy needed to incorporate Sm^{3+} ions into octahedral sites during synthesis is now used for crystallite growth.

3.2 Electrical Properties

3.2.1 Dielectric Constant and Dielectric Loss

The room temperature frequency dependence of the dielectric constant (the real and the imaginary parts) of $NiFe_{2-x}Sm_xO_4$ ceramics in the frequency range 1 to 10^6 Hz are shown in Figs. 4 and 5. Two types of variations may be detected from the figures, one being the variance in dielectric permittivity (ε' and ε'') with the frequency applied and the other being with the composition of samarium ions. The real as well as the imaginary parts of dielectric constants are seen to decrease with increasing frequency. At lower frequencies, this decline is found to be rapid and sluggish at higher frequencies. The higher value of dielectric constants at the low-frequency region may be caused by the presence of all sorts of polarization (electronic, atomic, orientational, and space charges). Koop's hypothesis describes the reduction in permittivity with frequency, which is that dielectric can be considered an inhomogeneous two-layer Maxwell-Wagner model type medium. According to this model, the dielectric structure includes conductive grains that are isolated by insulating the boundaries of grain. The influence of grain boundaries is dominant over grain at lower frequencies. When grain boundaries are strongly resistive, the electrons enter the grain boundary by jumping and piling up and thereby creating a polarization that is extremely permittivity. Nevertheless, when the frequency increases, there is a drop in the permittivity; the electrons on the grain boundaries usually change their direction of motion at higher frequencies. It reduces the chance of electrons

Table 1 Structural parameters: lattice parameters, volume, density, phase fraction, crystallite size, etc., of pure and Sm-doped $NiFe_2O_4$ ceramics using Rietveld refinement of X-ray diffraction

Parameters	$x = 0.0$	$x = 0.50$		$x = 0.10$		$x = 0.15$		$x = 0.20$		$x = 0.25$	
	Phase	Phase		Phase		Phase		Phase		Phase	
	NF	NF	SmF	NF	SmF	NF	SmF	NF	SmF	NF	SmF
Space group	*Fd3m*	*Fd3m*	*Pbnm*	*Fd3m*	*Pbnm*	*Fd3m*	*Pbnm*	*Fd3m*	*Pbnm*	*Fd3m*	*Pbnm*
a	8.3372	8.3384	5.4033	8.3374	5.4001	8.3384	5.4011	8.3374	5.4005	8.3375	5.4005
b	8.3372	8.3384	5.5836	8.3374	5.5854	8.3384	5.5868	8.3374	5.5859	8.3375	5.5862
c	8.3372	8.3384	7.7076	8.3374	7.7064	8.3384	7.7064	8.3374	7.7055	8.3375	7.7055
Volume	579.50	579.75	232.54	579.54	232.44	579.75	232.56	579.55	232.45	579.57	232.46
Density (in g/cm^2)	5.47	5.47	6.80	5.551	6.915	5.62	6.94	5.626	7.014	5.642	7.285
Phase fraction	100	96.75	3.25	91.66	8.34	86.14	13.86	81.18	18.82	74.04	25.96
Crystallite size (in nm)	87.02	101	67.43	101.73	70.56	97.34	71.71	84.97	71.94	85.71	70.08
R_f	4.76	3.76	33.92	3.682	24.27	4.093	17.16	4.012	14.89	5.755	10.16
R_{brag}	3.87	3.36	35.99	3.454	23.03	4.67	15.40	5.170	13.35	7.306	10.80
R_{WP}	20.9	21.80		22.6		23.9		23.6		24.8	
R_{exp}	19.16	20.63		21.04		22.66		20.97		21.19	
R_p	38.0	37.70		37.3		37.2		35.9		35.2	
Zero point	− 0.0148	− 0.0200		− 0.0615		− 0.0155		− 0.0217		− 0.0213	
GOF	1.2	1.1		1.1		1.1		1.2		1.2	
χ^2	1.19	1.12		1.16		1.22		1.27		1.37	

crossing the grain boundary, and,= as a result, the permittivity declines [17]. From Fig. 4, it is quite clear that the frequency-dependent dielectric permittivity of the real part increases for the concentration of samarium ($x = 0.05$) but decreases sharply for a higher concentration of Sm^{3+} ions. The value of the real dielectric constant of 2.5% Sm-doped (at $x = 0.05$) nickel ferrite is much higher as compared with those of other ceramics. This could be ascribed to the increase in the amount of Fe^{3+} ions at the octahedral site. The doping of Sm3+ ions migrate Ni^{2+} ions to the tetrahedral sites to relax the strain, and

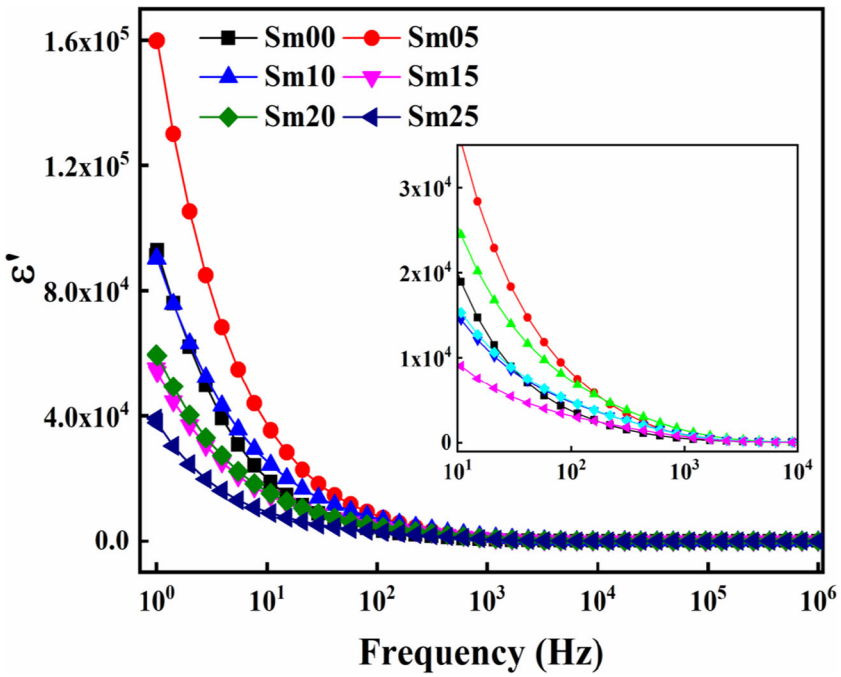

Fig. 4 Variation of the real part of dielectric constant with frequency

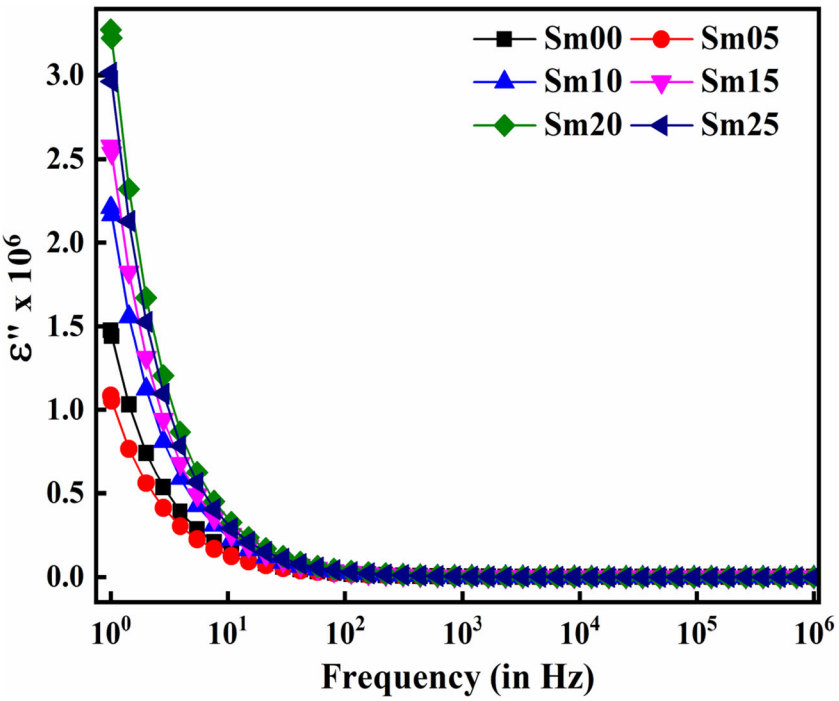

Fig. 5 Variation of the imaginary part of dielectric permittivity with frequency

equal amounts of iron ions are migrating from tetrahedral to octahedral sites, and therefore, there is an increment in hopping of electrons in octahedral sites from $Fe^{2+} \leftrightarrow Fe^{3+}$ ions; hence, the real part of dielectric permittivity increased [21]. For higher doping concentration, the value of the real part of dielectric permittivity decreases. This could be caused by the non-incorporation of higher Sm^{3+} content into $NiFe_2O_4$, and the transport of Fe^{3+} ions from the tetrahedral to the octahedral sites are slightly restricted. Since the ionic radius of Sm^{3+} is much higher as compared with that of Fe^{3+} ion. Thus, there was the formation of a large number of $SmFeO_3$ secondary phases in $NiFe_{2-x}Sm_xO4$. Now, due to this secondary phase $SmFeO_3$, Sm^{3+} ions replace the Fe^{3+} ions at octahedral sites which further brings down the hopping rate of electrons between $Fe^{2+} \leftrightarrow Fe^{3+}$, and the real part of dielectric permittivity decreased [22]. For the power application of the ferrites, a high dielectric constant is desired. Therefore, for application purposes, the concentrations of Sm^{3+} must be kept low.

Energy loss is commonly defined as a dielectric loss factor and refers to tan δ, where δ constitutes a phase difference betwixt the applied electric field and the induced current. Polarization is located behind the applied alternating field and tangent dielectric loss occurrence can be caused by grain boundary, impurity, crystal defect, and structural inhomogeneity in ferrites [22]. Figure 6 also demonstrates variations in the dielectric loss at room temperature with frequency ranges of 1 to 1 MHz. It has been perceived that the dielectric loss decreases with shoulder-like behavior as the frequency increases. The loss was found to be extreme at lower frequencies, and it drops at higher frequencies with one resonance (relaxation) peak at around 3 kHz for all the samples. This is caused by the jump of the electron between the Fe^{2+} and Fe^{3+} sites. If the frequency of the externally applied electric field is roughly equivalent to the frequency of the charging carriers being hopped, then the resonance condition is achieved. This resonance behavior was exhibited by all the samples emphasized in the inset of Fig. 6. The rationale for the moving resonance peaks with the dopant (Sm^{3+}) material to higher frequencies is due to reduced oxygen vacancies as Sm^{3+} ions replace Fe^{3+} ions. This type of resonance behavior can also be caused by the distortion of the lattice produced by the greater Sm^{3+} ion radii. The value of tan δ first decreases and then increases by adding Sm concentration. It is found that all other Sm-doped samples except for $x = 0.05$ exhibit high dielectric loss compared with pure $NiFe_2O_4$. Thus, it can currently be assumed that at the concentration of $x = 0.05$, the ceramic confined the maximum dielectric constant value with a tangent of minimal loss. Thus, sample with $x = 0.05$ data in $NiFe_2O_4$ is perfect for the point of view of applications such as high-frequency data reading/writing in electronic structure and also used in memories, transformer, and inductor cores [23, 24].

3.2.2 AC Conductivity

The AC conductivity variation with frequency (1 to 1 MHz) for $NiFe_{2-x}Sm_xO4$ ferrites are shown in Fig. 7. The conductivity spectra have been divided into three different regions. In region I ($1–10^2$ Hz), the sample does not respond to the applied frequency. This region is known as the plateau region,

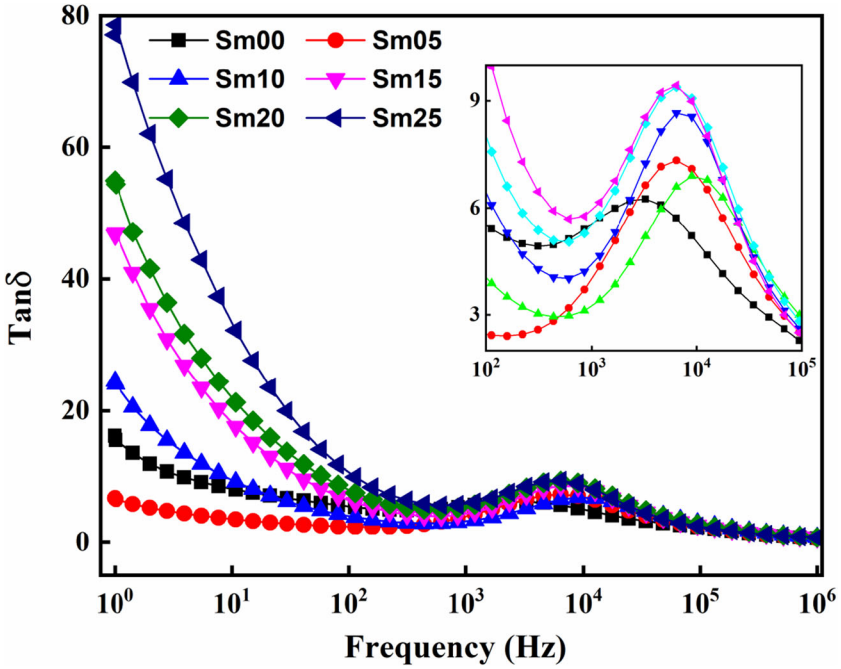

Fig. 6 Variation of dielectric loss with frequency

and the value of constant conductivity is called DC conductivity. Region I corresponds to grain boundary contribution. In region II (10^2–10^4 Hz), the σ_{ac} curve depends on frequency as both increase simultaneously and is also called dispersion at moderate frequency. Whereas in region III (10^4–10^6Hz), the increase in the σ_{ac} curve is sharp in comparison with region II depicting bound charge carriers. This region is known as the second plateau region and corresponds to the conductions of grains followed by high-frequency dispersion. The frequency-independent plateau region (DC conductivity) at lower frequency is assigned to the long-range translation movement of ions. The jump relaxation model can be explained [25]. In this model, the hopping of an ion from one site to another nearby empty site leads to the material's DC conductivity at lower frequencies. Conduction takes place in the dispersion region via the hopping mechanism of the charging carriers. The frequency of hopping is the frequency at which the dispersion region is observed. Conductivity increases at higher frequencies, due to forward and backward hopping along with ion relaxation [26]. For such a case, the high frequency increases the electronic jumps between the localized states.

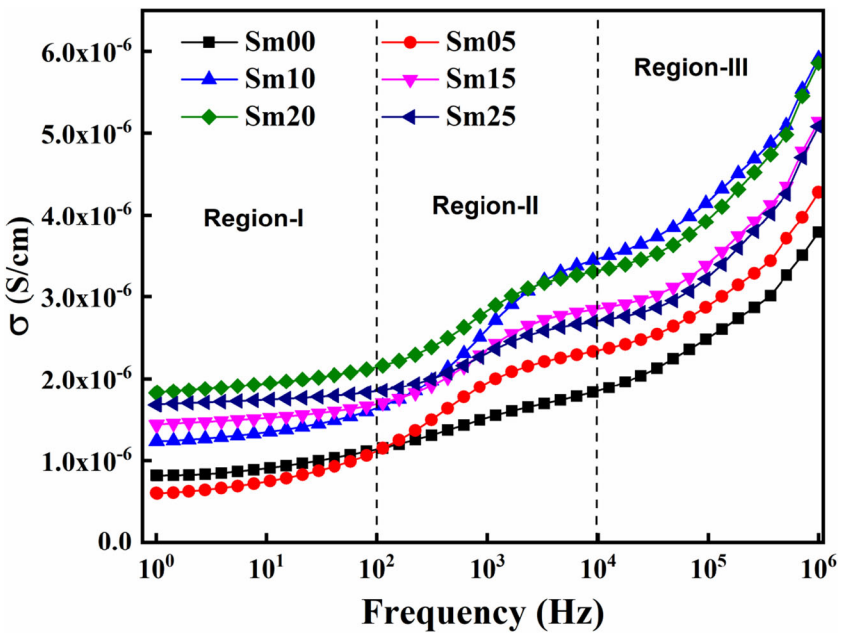

Fig. 7 Variation of AC conductivity with frequency

In most materials, the value of conductivity of ceramics is evaluated from the theoretical fitting of AC conductivity using Jonscher's universal power law [27]

$$\sigma_{ac} = \sigma_{dc} + A\omega^{n}$$

where σ_{ac} represents AC conductivity, σ_{dc} is the dc limit of the conductivity, $A\omega^{n}$ refers to the transport properties of the charging carriers (that could be polarons, ions, and electrons), A refers to the pre-exponential factor which determines the polarizability strength and ω refers to the angular frequency and n is the fractional exponent (lies in the range of 0–1) which provides the information about the degree of correlation between ion hops in the conduction process. Parameters A and s depend on the temperature of the material and its nature. By analyzing the results, there are two plateau regions for the conductivity spectrum for all the samples, which correspond to the grain boundary (at a lower frequency) and the contribution of grain (at a higher frequency). The spectrum is not adequate for explaining the mechanism of conduction using single power law. Consequently, a modification in Jonscher's power law [25] could explain the conductivity behavior in all samples:

$$\sigma_{ac} = \sigma_{dc} + A_1\omega^{n1} + A_2\omega^{n2}$$

where σ_{ac} represents total conductivity; σ_{dc} is the DC conductivity; A_1, n_1, A_2, and n_2 are the pre-exponential and the fractional components for grain and grain boundaries (for regions I and II), respectively. The conductivity spectra have been well equipped with the modified Jonscher's power law are shown in Fig. 8, and the values of the extracted parameters are enlisted in Table 2. With rising frequency, AC conductivity values of all the samples were found to grow. This conductivity process in ferrites is responsible owing to the exchange of electrons between Fe^{2+} and Fe^{3+} and the presence of oxygen vacancies. If the frequency is raised, the conductive grains become more active in the sample. The electrons were then jumped in Fe^{2+} and Fe^{3+} ions. Therefore, the AC conductivity will also increase with rising frequency. Figure 7 also shows the compositional variability of rare earth ion (Sm^{3+})–doped nickel ferrite conductivity spectra and found that $NiFe_{2-x}Sm_xO_4$ conductivity increases with an increase in Sm^{3+} material. This is due to the small polaron hopping [28, 29].

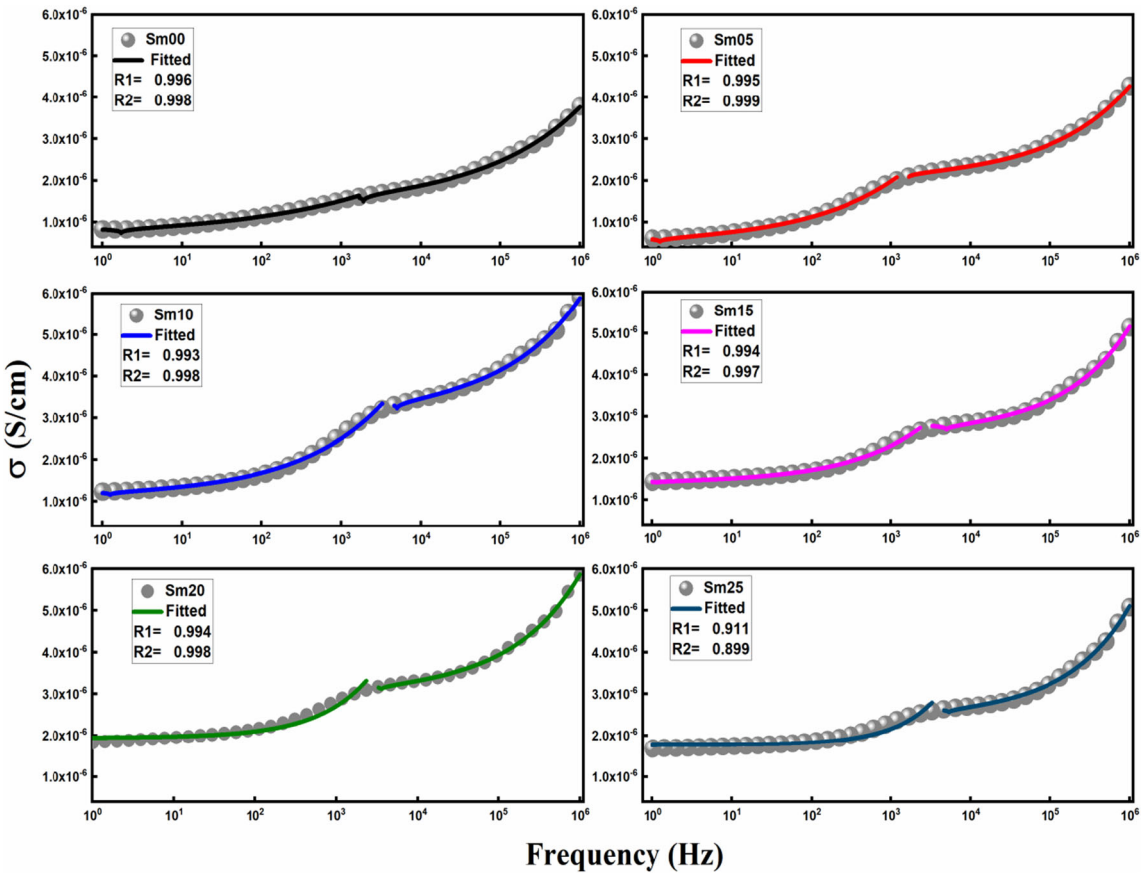

Fig. 8 Conductivity data fitted using modified Jonscher's power law

Table 2 Fitted different parameters using the modified power law of Jonscher's for pure and Sm-doped samples

Sample	σ_{dc} (S/cm)	A (polarizability strength)		S (degree of correlation)	
		$A1$	$A2$	S_1	S_2
Sm00	7.116×10^{-7}	1.707×10^{-7}	1.471×10^{-8}	0.278	0.365
Sm05	5.203×10^{-7}	1.043×10^{-7}	5.093×10^{-9}	0.381	0.439
Sm10	1.152×10^{-6}	8.171×10^{-8}	5.225×10^{-9}	0.406	0.451
Sm15	1.416×10^{-6}	3.419×10^{-8}	1.627×10^{-9}	0.470	0.530
Sm20	1.942×10^{-6}	6.626×10^{-9}	2.132×10^{-9}	0.695	0.518
Sm25	1.766×10^{-6}	1.403×10^{-9}	1.095×10^{-9}	0.8149	0.561

3.2.3 Impedance Analysis

The electro-ceramics have the main electrical properties because of the inter-grain, intra-grain, and electrode effects. Grain and grain boundaries are generally affected by a polycrystalline material. In polycrystalline materials, the inter-grain boundaries are defective areas in which deviations from the stoichiometry of oxygen and separation of dopants, impurities, or subsequent phases could occur [30]. Impedance analysis is a powerful tool to completely understand the electrical properties of heterogeneous materials. Complex impedance in the form of $Z = Z' + Z''$, which provides the details for both resistive and reactive contributions to conductivity on the application of the AC field. The resistive component acts as a real part Z', and the reactive component acts as an imaginary part Z''. To find the entire contribution of the microstructure resistance, owing to the grain or grain boundaries, a diagram is constructed between resistive and reactive parts of complex impedance. This scenario is referred to as the Nyquist or Cole-Cole plot. This constructed diagram gives three half circles, which generally represent the grain, grain boundaries, and electrode effect. Although ferrite substance contains a lack of an ionic polarization so that only two half circles are feasible owing to the contribution of grain and grain boundaries. Here, the key purpose to analyze the conduction process is attributable to either the grain or grain boundary or both of them [28]. Figure 9 shows the variations of the resistive part (Z') of impedance with applied frequency, for the pure and Sm-doped $NiFe_2O_4$. At lower frequencies, the magnitude of resistive part Z' is higher, and monotonous decreases in the high-frequency regime. This suggests an improvement in AC conductivity as the frequency rises. Figure 9 also indicates that various Z' curves coincide with higher frequency values for all of the samples. That may be because the space charge is released, and the barrier potential is reduced inside the material [30]. Figure 10 shows the reactive part (Z'') as a function of applied frequency at various dopings of samarium ion. For all of the compositions, 2 peaks related to the grain boundary and the grains were remarked in the low- and high-frequency regimes. The value of Z'' increases to maximum (Z''_{max}), after

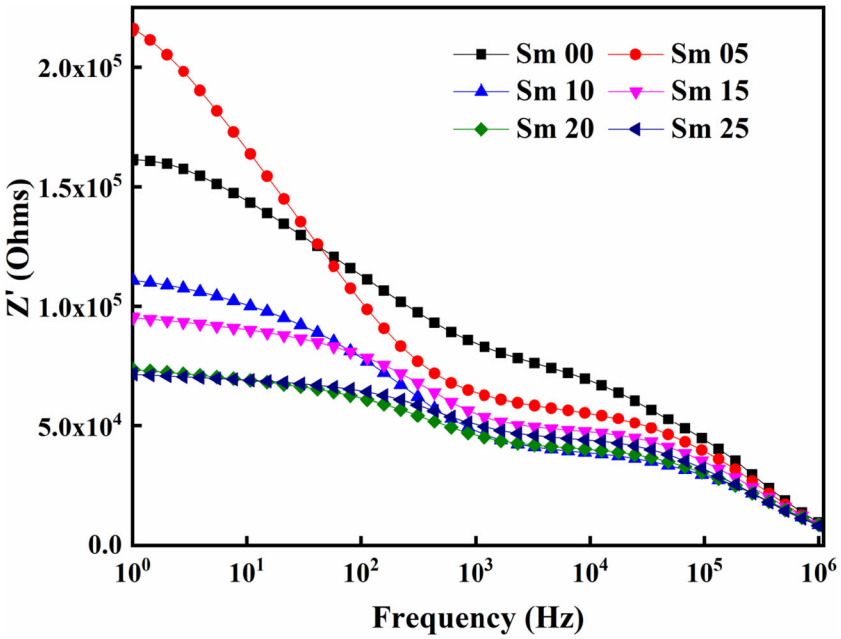

Fig. 9 Variation of the real part of impedance with frequency

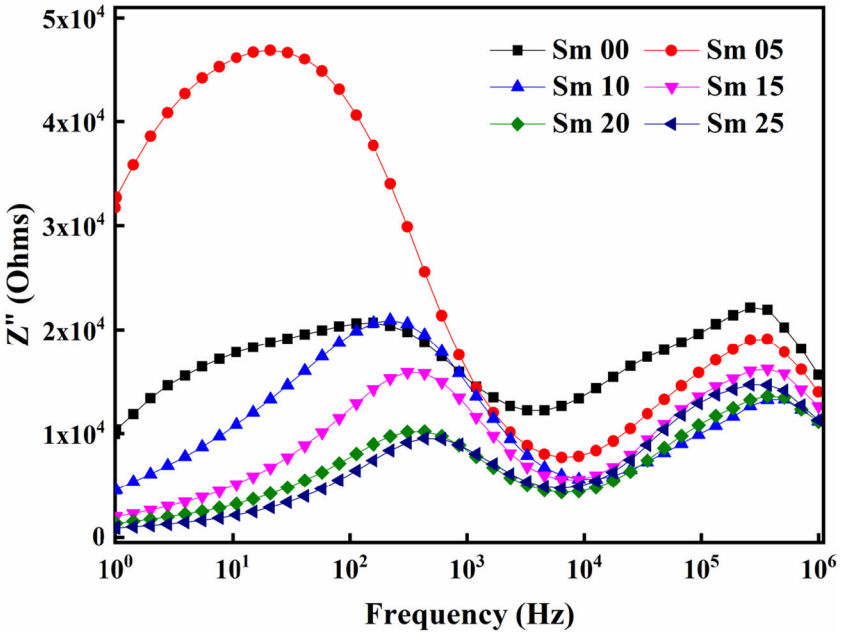

Fig. 10 Variation of the imaginary part of impedance with frequency

which the value begins to decline. This relaxation behavior is due to the presence of immobile species [31], hopping procedure of the charge carriers, and intrinsically domination of small polaron in the polycrystalline substances. Further, the Z''_{max} is pronounced to relocate to higher frequencies with improving doping concentration except for $x = 0.05$. The declined magnitude of Z''_{max} with doping concentration indicates a decline in the resistive property. Again, the merger of various Z'' curves at high frequencies is a symbol of space charge accumulation in the materials. Since the height of Z'' peak $(Z''_{max}) = R/2$, the Z'' graph is linked to the most resistive component of the material. Bulk capacitances (C_b) of the samples were described from the peaks of semicircles, using the ratio $\omega_{max} C_b R_b = 1$ [32]. The relaxation time is equal to the reciprocal of $\omega_{max.}$ The reactive component of impedance versus the resistive portion of impedance is constructed through a wide variety of frequencies (1–1 MHz), which are shown in Fig. 11. All the Nyquist plots for pure and doped samples compose of two overlapping depressed semicircles at low and high frequencies which assist to distinguish the resistance of grain and grain boundary and interfacial resistance of conducting electrode. The semicircle appearing at a low-frequency region is due to grain boundaries, which takes place due to parallel combination of the grain boundary resistance R_{gb} and grain capacitance C_{gb} of the material, and the other one semicircle at a higher frequency region belongs to bulk (grain), which takes place due to parallel combination of the grain resistance (R_g) and grain boundary capacitance (C_g) of the material [16, 21]. Furthermore, there is no other relaxation tool like the electrode effect that has been noticed, which is normally present on the lower frequency portion of the continuum of impedance. The data depicted in Table 3 was examined by the reactive part (Z'') versus frequency curve to evaluate various parameters including resistance of grains (R_g), the relaxation time of grains (τ_g), the capacitance of grains (C_g), resistance at grain boundaries (R_{gb}), the capacitance at grain boundaries (C_{gb}), and relaxation time of grains (τ_g), at room temperature. The resistances (R_g and R_{gb}) could be also obtained by intersections of the circular arc on x-axis (Z') and the capacitances (C_g and C_{gb}) were estimated by taking out the height of the circular arcs [28]. The magnitude of resistance R_g and R_{gb} (diameter of the semicircle in the Cole-Cole plot) initially increases at $x = 0.05$ but decreases for a higher concentration of samarium ions which indicates that the overall DC conduction of the Sm^{3+}-doped nickel ferrite nanoparticles increases. At a lower concentration (at $x =$ 0.05 and 0.1), the resistance of grain boundary is higher as compared with the resistance of grain. Through the Cole-Cole plot, it has been found that the diameter of the grain boundary region is greater as compared with the diameter of the grain region. This fact suggests that when Sm ions are substituted in the $NiFe_2O_4$, the process of conduction is primarily caused by grain boundaries. This implies that the contribution at the grain boundaries is greater than the contribution from the grain because of the small crystallite effects. All the semicircles exhibit a certain degree of depression in the place of centered at the Z' axis. This is because of the spread of relaxation time. This form of machine relaxation refers to the relaxation of the non-Debye type [28, 30]

3.3 Ferroelectrical Study

Generally, the dielectric is a substance in which the electrons are very closely bound together. The electric charges in the

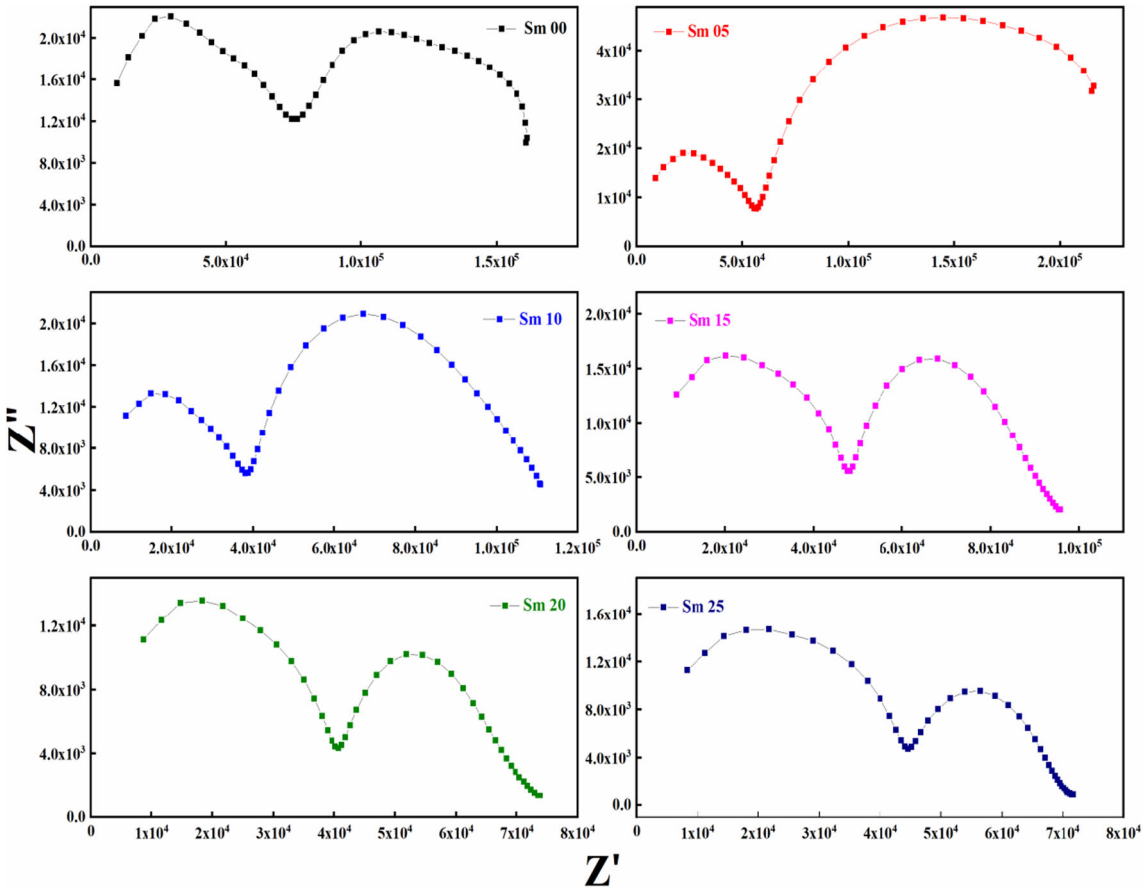

Fig. 11 Nyquist or Cole-Cole plots for samarium (Sm^{3+})-doped $NiFe_2O_4$

dielectrics can react to an applied electric field by adjusting the dielectric polarization. The polarization of pure and doped nickel ferrite against the electric field (*P-E*) was assessed in two separate ways, firstly with silver paint and secondly without silver paint. Starting with silver paint, we have applied a maximum electric field of ~ 1 kV/cm (50 Hz) at room temperature and are displayed in Fig. 12. It looks nearly circular. We observe maximum polarization (P_{max}) at zero electric fields, whereas the value of P_{max} is equal to remnant polarization (+ P_r). In this case, charging carriers do not tend to produce dipoles with the electric field being applied to that. Instead, at the maximum electric field (~ 0.72 kV/cm), polarization is zero. Such a polarization loop does not demonstrate real electrical polarization and is due to the conductive effect [33].

Without silver paint, we have applied a maximum electric field of order 3 kV/cm with 1000 Hz frequency at room temperature and is displayed in Fig. 13. In this field and frequency range, the entire sample shows a non-linear PE loop with very weak remnant polarization. However, we observe for pristine nickel ferrite, the value of P_{max} (~ 0.0024 μC/cm^2) is not zero at the higher electric field (3 kV/cm) without a coating of silver paste at 300 V. The sample is still semi-conductive in these observations but is made more conductive by the silver paint [33].

Table 3 Resistance of grains and grain boundaries (R_g and R_{gb}), the capacitance of grains and grain boundaries (C_g and C_{gb}), relaxation time of grains and grain boundaries (τ_g and τ_{gb}), etc., measured by impedance study

Sample	R_g (KΩ)	R_{gb} (KΩ)	C_g (nF)	C_{gb} (nF)	τ_g (S)	τ_{gb} (S)	ω_g (Hz)	ω_{gb} (Hz)
Sm00	44,292	41,318	0.08078	140.702	3.57814E−06	5.814E−03	279,475	172.01
Sm05	38,346	94,363	0.0733	493.429	2.81171E−06	46.562E−03	355,654	21.47
Sm10	29,922	42,310	0.1165	102.304	3.48849E−06	4.328E−03	286,657	231.02
Sm15	32,166	31,904	0.0849	88.1376	2.73259E−06	2.812E−03	365,953	355.62
Sm20	27,212	21,236	0.0951	139.749	2.58916E−06	2.968E−03	386,226	336.95
Sm25	26,558	19,750	0.0863	111.529	2.29211E−06	2.203E−03	436,280	453.99

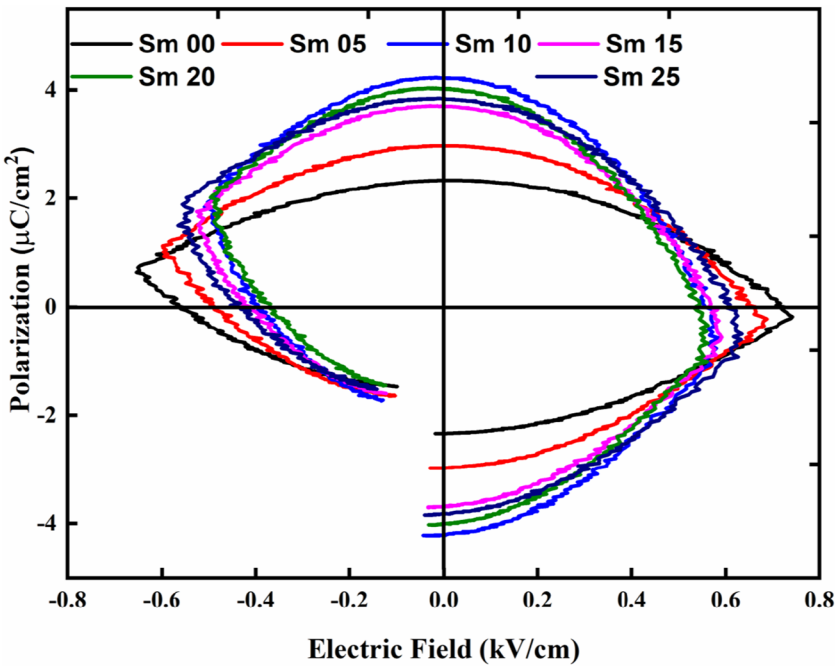

Fig. 12 PE hysteresis loop with silver paint at 50 Hz frequency

From Figs. 12 and 13, it has been clear that with increasing doping concentration, there is a steep enhancement found in remnant polarization (P_r) and coercive field (E_c), which are shown in Table 4. The remnant polarization in samarium-doped samples is increased in comparison with the pure one, thereby increasing ferroelectric properties in the doped sample. *P-E* loops demonstrate that doping renders the most resistive nature of loops. As in many of the rare earth ions, Sm^{3+} ion substitution in NF will suppress oxygen vacancies because of its higher ionic radius and enhancement of impurity of the secondary phase of $SmFeO_3$ in samples. Consequently, the current leakage density decreases (Fig. 14 confirmed), and the ferroelectric property enhances. The leakage current density was widely assumed to play a significant role with regards to the ferroelectric property. Therefore, further study would also concentrate on the behavior of leakage current.

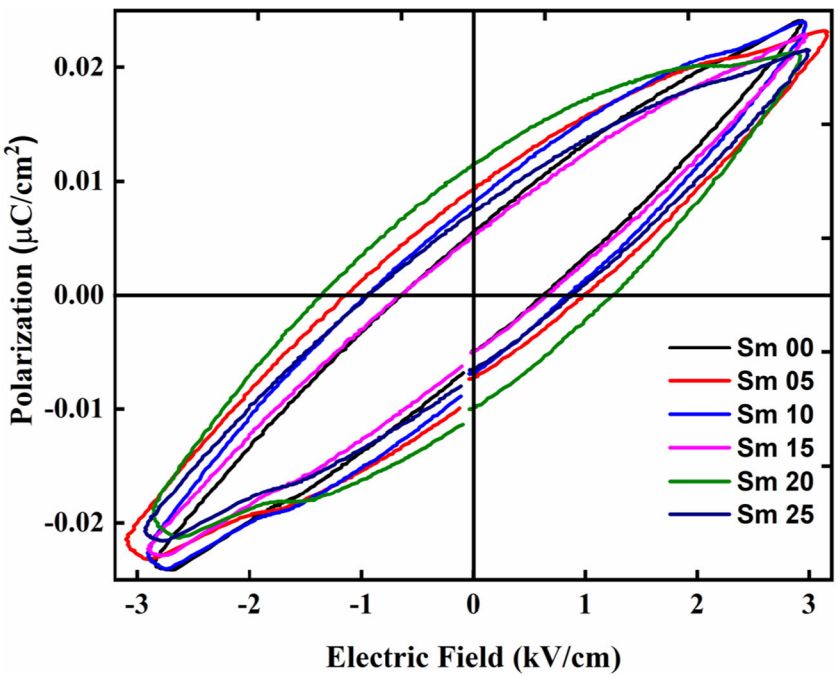

Fig. 13 PE hysteresis loop without silver paint at 1000 Hz frequency

Table 4 Dielectric constant and loss tangent, polarization, and coercivity of pure and Sm-doped samples using *P-E* and dielectric measurement

Sample	Dielectric constant	Dielectric loss	P_{max} (μC/cm^2)	$+P_r$ (μC/cm^2)	$-P_r$ (μC/cm^2)	Coercivity (kV/cm)	Loop area
At 50 Hz							
Sm00	6165	6.17	-1.77×10^{-1}	2.33	−1.47	0.72045	3.87×10^{2}
Sm05	13,000	2.62	-2.20×10^{-1}	2.97	−1.65	0.6623	4.37×10^{2}
Sm10	10,582	5.15	-5.87×10^{-1}	4.22	−1.74	0.5594	4.56×10^{2}
Sm15	6581	8.87	-5.63×10^{-1}	3.69	−1.60	0.5744	4.38×10^{2}
Sm20	6761	10.92	-3.41×10^{-1}	4.02	−1.46	0.5428	4.36×10^{2}
Sm25	4165	15.43	-5.3×10^{-1}	3.83	−1.52	0.6075	4.35×10^{2}
At 1000 Hz							
Sm00	493	5.53	2.41×10^{-2}	5.57×10^{-3}	-6.83×10^{-3}	0.5154	5.78
Sm05	893	4.00	2.31×10^{-2}	9.30×10^{-3}	-9.92×10^{-3}	0.8760	8.10
Sm10	1457	3.22	2.37×10^{-2}	8.10×10^{-3}	-8.88×10^{-3}	0.7400	7.54
Sm15	977	4.40	2.27×10^{-2}	5.24×10^{-3}	-6.25×10^{-3}	0.5517	4.66
Sm20	938	5.51	2.10×10^{-2}	9.93×10^{-3}	-11.4×10^{-3}	1.1364	8.09
Sm25	708	5.96	2.15×10^{-2}	7.32×10^{-3}	-7.99×10^{-3}	0.7758	5.69

3.4 Leakage Current Behavior (*J-E* Measurement)

Figure 14 indicates the leakage current density (*J*) depending/based on the applied electric field (*E*) at different doping concentrations of samarium (Sm^{3+}) ion. From Fig. 14, the Sm^{3+} doping helps in reducing the leakage current. These reduced values of leakage current densities are given in Table 5. This reduced leakage current density shows that the samples have high resistivity with increasing doping concentration in pristine $NiFe_2O_4$. The leakage current of $NiFe_2O_4$ is produced as a known source from oxygen vacancies, which is primarily caused by the volatilization of Fe^{3+}. The substitution can regulate Fe^{3+} volatilization and reduce the vacancies in oxygen, especially the substitution of rare earth ion and thus reducing the density of the leakage current [34]. With the result of the incorporation of Sm modifier in the Fe site, consequently, we thus assume that many effects contribute to the source of decreased leakage current in the pristine nickel ferrite and doped samples, including the existence of $SmFeO_3$ phases in the lattice, decreases in oxygen vacancies, stabilizing oxidation state (Fe^{3+}) and smooth surface micro-structure with dense grains. This kind of *J-E* response may be interpreted according to the process of space charge-limited current (SCLC) conduction [35]. A trap-controlled SCLC is

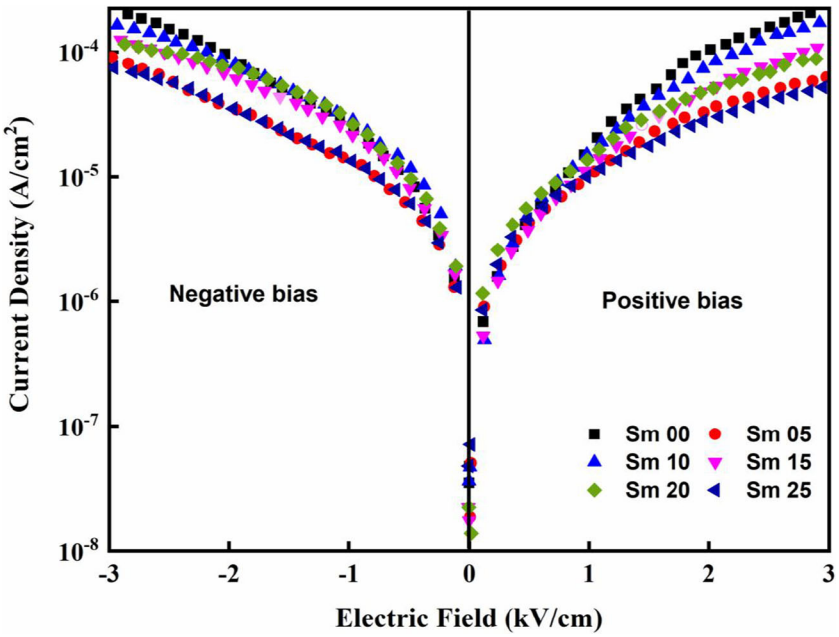

Fig. 14 Leakage current density as a function of the applied electric field

Table 5 Leakage or conduction mechanisms for pristine and Sm-doped nickel ferrites using double logarithmic plot [log(J) vs log(E)]

Sample name	Leakage current (A/cm^2)	First slope S_1	Second slope S_2	Threshold field (kV/cm)
Sm00	2.18×10^{-4}	1.25 ± 0.05	2.32 ± 0.04	0.54
Sm05	6.40×10^{-5}	1.81 ± 0.05	1.52 ± 0.01	1.17
Sm10	1.75×10^{-4}	1.97 ± 0.05	2.29 ± 0.03	1.09
Sm15	1.07×10^{-4}	1.98 ± 0.01	2.08 ± 0.02	1.13
Sm20	8.96×10^{-5}	2.12 ± 0.05	1.62 ± 0.02	1.12
Sm25	5.10×10^{-5}	1.27 ± 0.01	1.56 ± 0.01	1.09

composed of three sections: (1) ohmic region ($I \propto V$), (2) Child's square law region ($I \propto V^2$), and (3) steep growth in the high field region. The conductive mechanism in the low field regime is controlled by the free electrons in the ceramics which is produced thermally. Once the field goes beyond the onset voltage of the square law, the density of electrons which are injected progressively goes beyond the concentration of the equilibrium and dominates the conduction. Region I-V^2 is classified as a trap unfilled region that has not been filled with trap, while the third region is also referred to as a trap-filled region that is filled with traps. In summary, the conduction of SCLC has been found in many different materials, and it is generally known that the defect-related traps, such as the oxygen vacancies, are generally correlated with the conduction of the SCLC. The SCLC signature is fairly confirmed by two regions of the discrete slopes when the distinctive function of I-V is constructed in a double logarithmic scale [36].

To investigate the type of leakage or conduction mechanisms for pristine and doped nickel ferrites, the leakage current density and an applied electric field was plotted as double logarithmic scale [log(J) vs log(E)] which are presented in Fig. 15. As one can see, the data can be divided into two regions (corresponding to low and high applied electric fields) and can be well fitted by two linear segments with

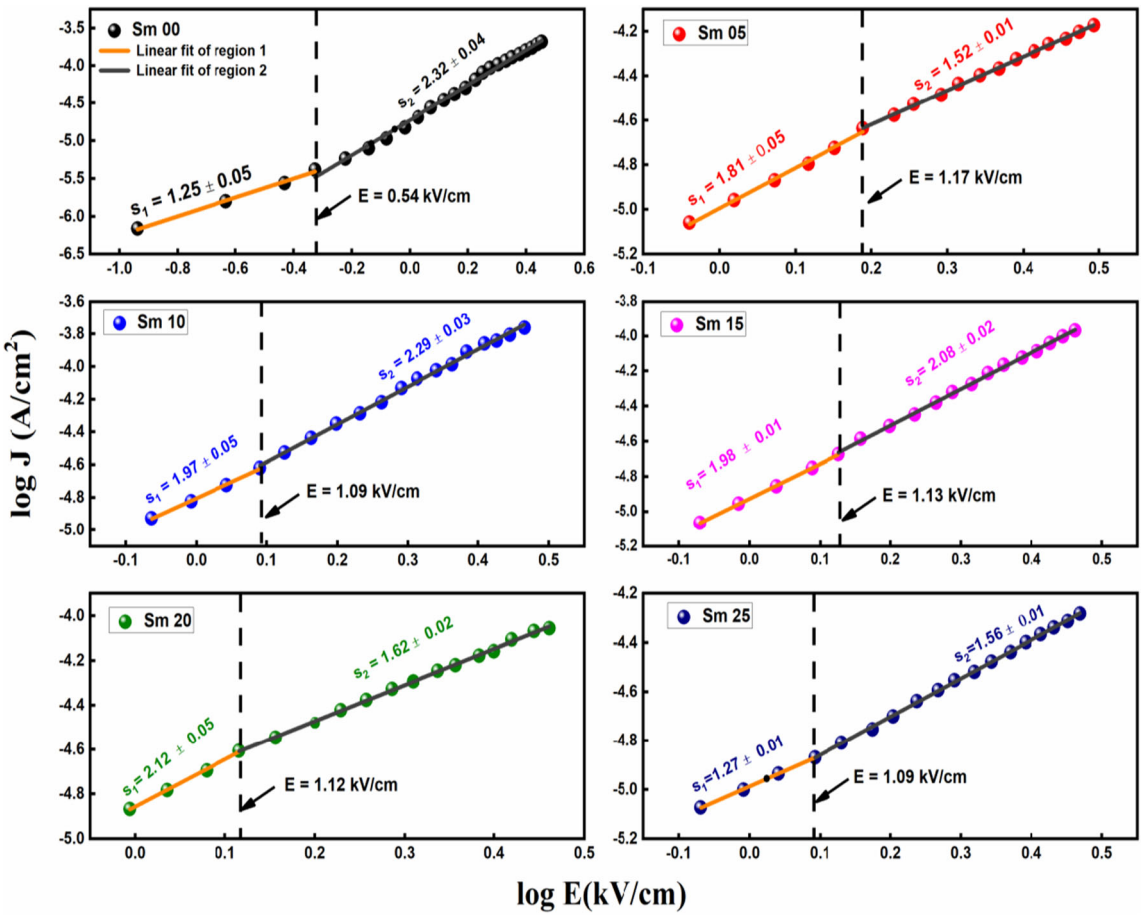

Fig. 15 log (J) versus log (E) characteristics of pure and doped $NiFe_2O_4$

distinct slopes. The value of these two slopes are given in Table 5 and also mentioned in Fig. 15. The slope m of these plots gives information about various leakage mechanisms contributing to the leakage behavior of the sample. These are the following mechanisms: (1) grain boundary limited conduction ($I \propto V^m$, $m < 1$); (2) ohmic conduction ($m = 1$); (3) trap-unfilled SCLC ($m = 2$); (4) the trap-filled limit (reached at voltage V_{TFL}, $m > 2$); and (5) trap-free SCLC ($m = 2$) [37]. Therefore, several *I-V* curves can be shown depending on the existence of material defects. For pristine nickel ferrite, the slope of ln E vs ln J curves is 1.25 ± 0.05 around 1 at low electric field (0.54 kV/cm) region which indicates the dominance of ohmic conduction. This suggests that the density of injected carrier n is small compared with the density of thermally stimulated free electrons n_0, and the injected carriers are distributed again with a propensity to preserve electric charge neutrality. But with the further increase of the electric field up to 3 kV/cm, the leakage current density J increases sharply, and the slope of the log E vs log J curves is 2.32 ± 0.04, which indicates that the leakage current conduction mechanism agrees well with trap-unfilled SCLC conduction mechanism at high field region. This suggests that in the presence of a sufficiently higher electric field, the density of free electrons by carrier injecting is higher than that of free electron density with thermal stimulation [38]. It is also observed from Fig. 15 and data are given in Table 5, at lower field regime (below threshold electric field $E < E_{tr}$), and initially, the value of slope S_1 is approximately 1.25 for the pure sample. With increasing doping concentration, there is an enhancement in the value of slope S_1. For $x = 0.20$, the value of the first slope reaches approximately 2.12 which is greater than two. This behavior (changing of slope from ~ 1 to ~ 2) could be due to a transition of the conduction mechanism from ohmic to SCLC. At a sufficiently high applied electric field, (above threshold electric field $E > E_{tr}$ regime), the value of slope S_2 is initially 2.32 for the pure sample. With increasing doping concentration, decay has been observed in the value of slope S_2. This could be due to a transition of the conduction mechanism from SCLC to ohmic. The key difference in the conduction activity of these ferrites is the difference in the E_{tr} threshold (minimum field needed to transition from the ohmic to the trap-unfilled SCLC) [34, 39]. An SCLC mechanism is typically related to free carriers trapped by vacancies in oxygen. When injected electron passes through samples, the thermal electrons are affected by traps, which are generated from oxygen vacancies. Due to a reduction in oxygen vacancies, the density of free carriers will be also reduced. When the density of the injected free carrier is less than the density generated by the free carrier, then ohmic conduction will become dominant. Because of the reduction in oxygen vacancies, at a higher field, samples have dominant ohmic conduction with doping concentrations.

4 Conclusion

Pristine and samarium-doped nickel ferrite ceramics with the formula $NiFe_{2-x}Sm_xO_4$ ($0.00 \leq x \leq 0.25$) were synthesized using self- ignited sol-gel autocombustion method. The structural information has been investigated by XRD which reveals that Sm enters the spinel lattice of nickel ferrite partially as a samarium ferrite orthorhombic phase ($SmFeO_3$) is detected in small proportions confirming that samarium has limited solubility in spinel lattice due to its higher ionic radius. Also, Rietveld refinement enables us to determine the amount of impurity phase presented in the samples. Phase fraction of the samarium ferrite is increased with doping concentration. Due to the maximum value of dielectric constant and minimal loss tangent with $x = 0.05$, data in nickel ferrite is good for application point of view such as high-frequency data reading/writing in the electronic structure and is also used in memories, transformer, and inductor core. All the samples show two plateau regions in the conductivity spectrum and are represented as the grain and grain boundaries. The Cole-Cole plot confirms that the process of conduction is mainly owing to the grain boundaries because the diameter of the grain boundary region is greater than that of the grain region. The enhanced ferroelectric properties are confirmed by the increased value of remnant polarization and reducing leakage current with doping. This kind of leakage current is based on SCLC.

Acknowledgments UGC-DAE-CSR, as an institute, is acknowledged for providing some of the experimental facilities for sample characterization. The authors sincerely thank Dr. M. Gupta of UGC-DAE-CSR, Indore, India, for providing the XRD facility. Thanks to Dr. V. R. Reddy of UGC-DAE-CSR, Indore, India, for providing *P-E* and *J-E* measurements, and Mr. Bhardwaj of UGC-DAE-CSR, Indore, India, is gratefully acknowledged for dielectric measurements and fruitful discussions.

Funding

Authors acknowledge the Ministry of Minority Affairs through UGC, Government of India, for providing financial support through Maulana Azad National Fellowship Scheme F1-17.1/2016-17/MANF-2015-17-MAD-55974 /(SAIII/Website).

Compliance with Ethical Standards

Competing Interest The authors declare that they have no competing interests.

References

1. Almessiere, M.A., Slimani, Y., Korkmaz, A.D., Taskhandi, N., Sertkol, M., Baykal, A., Shirsath, S.E., Ercan, Ozçelik, B.: Sonochemical synthesis of Eu3+ substituted CoFe2O4 nanoparticles and their structural, optical and magnetic properties. Ultrason. Sonochem. **58**, 104621 (2019). https://doi.org/10.1016/j.ultsonch.2019.104621
2. Albetran, H., Slimani, Y., Almessiere, M.A., Alahmari, F., Shirsath, S.E., Akhtar, S., Low, I.M., Baykal, A., Ercan, I.:

Synthesis, characterization and magnetic investigation of Er-substituted electrospun NiFe2O4 nanofibers. Phys. Scr. **95**, 075801 (2020). https://doi.org/10.1088/1402-4896/ab8b7d
3. Korkmaz, A.D., Güner, S., Slimani, Y., Gungunes, H., Amir, M., Manikandan, A., Baykal, A.: Microstructural, optical, and magnetic properties of vanadium-substituted nickel spinel nanoferrites. J. Supercond. Nov. Magn. **32**, 1057 (2019). https://doi.org/10.1007/s10948-018-4793-6
4. Slimani, Y., Almessiere, M.A., Korkmaz, A.D., Guner, S., Güngüneş, H., Sertkol, M., Manikandan, A., Yildiz, A., Akhtar, S., Shirsath, S.E., Baykal, A.: $Ni_{0.4}Cu_{0.2}Zn_{0.4}Tb_xFe_{2-x}O_4$ nanospinel ferrites: ultrasonic synthesis and physical properties. Ultrason. Sonochem. **59**, 104757 (2019). https://doi.org/10.1016/j.ultsonch.2019.104757
5. Sutka, A., Mezinskis, G.: Sol-Gel Auto-Combustion Synthesis of Spinel-Type Ferrite Nanomaterials. **6**, 128–141 (2012). https://doi.org/10.1007/s11706-012-0167-3
6. Akhtar, S., Rehman, S., Almessiere, M.A., Khan, F.A., Slimani, Y., Baykal, A.: Synthesis of $Mn_{0.5}$ $Zn_{0.5}$ Smx Eux $Fe_{1.8}$–2_x O_4 nanoparticles via the hydrothermal approach induced anti-cancer and anti-bacterial activities. Nanomaterials. **9**, (2019). https://doi.org/10.3390/nano9111635
7. Sartaj Aziz, H., Ali Khan, R., Shah, F., Ismail, B., Nisar, J., Mujtaba Shah, S., Rahim, A., Rahman Khan, A.: Improved electrical, dielectric and magnetic properties of Al-Sm co-doped $NiFe_2O_4$ spinel ferrites nanoparticles. Mater. Sci. Eng. B Solid State Mater. Adv. Technol. **243**, 47 (2019). https://doi.org/10.1016/j.mseb.2019.03.021
8. Ghosh, M.P., Mukherjee, S.: Disordered surface spins induced large exchange anisotropy in single-phase Sm3+ ions substituted nickel ferrite nanoparticles. J. Magn. Magn. Mater. **489**, 165320 (2019). https://doi.org/10.1016/j.jmmm.2019.165320
9. Almessiere, M.A., Slimani, Y., Güngüneş, H., Ali, S., Manikandan, A., Ercan, I., Baykal, A., Trukhanov, A.V.: Magnetic attributes of NiFe2O4 nanoparticles: influence of dysprosium ions (Dy3+) substitution. Nanomaterials. **9**, (2019). https://doi.org/10.3390/nano9060820
10. Ahmad, T., Lone, I.H., Ansari, S.G., Ahmed, J., Ahamad, T., Alshehri, S.M.: Multifunctional properties and applications of yttrium ferrite nanoparticles prepared by citrate precursor route. Mater. Des. **126**, 331 (2017). https://doi.org/10.1016/j.matdes.2017.04.034
11. Van Aken, B.B., Palstra, T.T.M., Filippetti, A., Spaldin, N.A.: The origin of ferroelectricity in magnetoelectric YMnO3. Nat. Mater. **3**, 164 (2004). https://doi.org/10.1038/nmat1080
12. Mishra, A., Khan, M., Jarabana, K.M., Bisen, S.: Structural, optical and EXAFS studies of nickel substituted copper ferrites Nano-particle by sol-gel auto combustion method. J. Phys. Conf. Ser. 755, 012044 (2016). http://iopscience.iop.org/1742-6596/755/1/012044
13. Khan, M., Mishra, A., Shukla, J., Sharma, P.: Structural, Optical and Electrical Properties of BaTiO3 -NiFe2O4 Based Multifunctional Composites. AIP Conference Proceedings. 2142 (2019). https://doi.org/10.1063/1.5122593
14. Khan, M., Mishra, A., Shukla, J., Bisen, S., Sharma, P.: Structural and Optical Properties of (1-x)BaTiO3-xNiFe2O4 Based Nano-Composites. AIP Conference Proceedings. 2115 (2019). https://doi.org/10.1063/1.5112946
15. Prodip, K.M., Mohammad, A.H., Mohammed, N.I.K., Shibendra, S.S.: Structural, magnetic and transport properties of samarium (Sm) doped Cu-Zn ferrites. Int. J. Phys. Sci. **14**, 21–29 (2019). https://doi.org/10.5897/ijps2018.4746
16. Rahman, M.T., Ramana, C.V.: Impedance spectroscopic characterization of gadolinium substituted cobalt ferrite ceramics. J. Appl. Phys. **116**, 164108 (2014). https://doi.org/10.1063/1.4896945
17. Joshi, S., Kumar, M., Chhoker, S., Srivastava, G., Jewariya, M., Singh, V.N.: Structural, magnetic, dielectric and optical properties of nickel ferrite nanoparticles synthesized by co-precipitation method. J. Mol. Struct. **1076**, 55–62 (2014). https://doi.org/10.1016/j.molstruc.2014.07.048
18. Dixit, G., Singh, J.P., Chen, C.L., Dong, C.L., Srivastava, R.C., Agrawal, H.M., Pong, W.F., Asokan, K.: Study of structural, morphological and electrical properties of Ce doped NiFe2O4 nanoparticles and their electronic structure investigation. J. Alloys Compd. **581**, 178–185 (2013). https://doi.org/10.1016/j.jallcom.2013.07.047
19. Dean, J.A.: Lange's handbook of chemistry. Mater. Manuf. Process. **5**, 687 (1990). https://doi.org/10.1080/10426919008953291
20. Hassanzadeh-Tabrizi, S.A., Behbahanian, S., Amighian, J.: Synthesis and magnetic properties of NiFe2-xSmxO4 nanopowder. J. Magn. Magn. Mater. **410**, 242 (2016). https://doi.org/10.1016/j.jmmm.2016.03.015
21. Murugesan, C., Chandrasekaran, G.: Impact of Gd3+ substitution on the structural, magnetic and electrical properties of cobalt ferrite nanoparticles. RSC Adv. **5**, 73714 (2015). https://doi.org/10.1039/c5ra14351a
22. Joshi, S., Kumar, M., Pandey, H., Singh, M., Pal, P.: Structural, magnetic and dielectric properties of Gd_{3+} substituted $NiFe_2O_4$ nanoparticles. J. Alloys Compd. **768**, 287–297 (2018). https://doi.org/10.1016/j.jallcom.2018.07.250
23. Sharma, N.D., Verma, M.K., Choudhary, N., Sharma, S., Singh, D.: Enhanced coercivity of $NiFe_{1-x}$ Dy_x CrO_4 ferrites synthesised by glycine-nitrate combustion method. Mater. Sci. Technol. **35**, 448–455 (2019). https://doi.org/10.1080/02670836.2019.1569836
24. Pervaiz, E., Gul, I.H.: Structural, electrical and magnetic studies of Gd $_{3+}$ doped cobalt ferrite. Nanoparticles. J. Curr. Eng. and Technol. **4**, 377–387 (2012). http://inpressco.com/category/ijcet
25. Sangwan, K.M., Ahlawat, N., Rani, S., Rani, S., Kundu, R.S.: Influence of Mn doping on electrical conductivity of lead free $BaZrTiO_3$ perovskite ceramic. Ceram. Int. **44**, 10315–10321 (2018). https://doi.org/10.1016/j.ceramint.2018.03.039
26. Yuvaraj, S., Layek, S., Vidyavathy, S.M., Yuvaraj, S., Meyrick, D., Selvan, R.K.: Electrical and magnetic properties of spherical $SmFeO_3$ synthesized by aspartic acid assisted combustion method. Mater. Res. Bull. **72**, 77 (2015). https://doi.org/10.1016/j.materresbull.2015.07.013
27. Bisen, S., Khan, M., Mishra, A.: Tailoring effect of large polaron hopping in the conduction mechanism of Ca-modified $BaTiO_3$ system. J. Mater. Sci. Mater. Electron. **31**, 9212 (2020). https://doi.org/10.1007/s10854-020-03452-1
28. Qindeel, R., Alonizan, N.H.: Structural, dielectric and magnetic properties of cobalt based spinel ferrites. Curr. Appl. Phys. **18**, 519–525 (2018). https://doi.org/10.1016/j.cap.2018.03.004
29. Koops, C.G.: On the dispersion of resistivity and dielectric constant of some semiconductors at audiofrequencies. Phys. Rev. **83**, 121 (1951). https://doi.org/10.1103/PhysRev.83.121
30. Bhargavi, G.N., Khare, A., Badapanda, T., Anwar, M.S., Brahme, N.: Electrical characterizations of $BaZr_{0.05}Ti_{0.95}O_3$ perovskite ceramic by impedance spectroscopy, electric modulus and conductivity. J. Mater. Sci. Mater. Electron. **28**, 16956–16964 (2017). https://doi.org/10.1007/s10854-017-7617-8
31. Tiwari, B., Choudhary, R.N.P.: Effect of Mn-substitution on structural and dielectric properties of $Pb(Zr_{0.65-x}Mn_xTi_{0.35})O_3$ ceramics. Solid State Sci. **11**, 219 (2009). https://doi.org/10.1016/j.solidstatesciences.2008.04.023
32. Naeem, A., Mahmood, A., Iqbal, Y., Ullah, A., Mahmood, T., Humayun, M.: Dielectric and impedance spectroscopic studies on $(Ba_{0.5}Sr_{0.5})Mn_x(Ti_{0.95}Fe_{0.05})_{1-x}O_3$ ceramics synthesized by using sol-gel method. J. Alloys Compd. **645**, 290–296 (2015). https://doi.org/10.1016/j.jallcom.2015.05.114
33. Choudhary, P., Saxena, P., Yadav, A., Sinha, A.K., Rai, V.N., Varshney, M.D., Mishra, A.: Weak ferroelectricity and leakage

current behavior of multiferroic CoCr2O4 nanomaterials. J. Supercond. Nov. Magn. **32**, 2639 (2019). https://doi.org/10.1007/s10948-019-5001-z

34. Mao, W., Yao, Q., Fan, Y., Wang, Y., Wang, X., Pu, Y., Li, X.: Combined experimental and theoretical investigation on modulation of multiferroic properties in $BiFeO_3$ ceramics induced by Dy and transition metals co-doping. J. Alloys Compd. **784**, 117 (2019). https://doi.org/10.1016/j.jallcom.2018.12.381
35. Kalita, P.K., Sarma, B.K., Das, H.L.: Space charge limited conduction in CdSe thin films. Bull. Mater. Sci. **26**, 613 (2003). https://doi.org/10.1007/bf02704325
36. Ye, C., Wu, J., He, G., Zhang, J., Deng, T., He, P., Wang, H.: Physical mechanism and performance factors of metal oxide based resistive switching memory: a review. J. Mater. Sci. Technol. **32**, 1 (2016). https://doi.org/10.1016/j.jmst.2015.10.018
37. Kwan, C.P., Street, M., Mahmood, A., Echtenkamp, W., Randle, M., He, K., Nathawat, J., Arabchigavkani, N., Barut, B., Yin, S., Dixit, R., Singisetti, U., Binek, C., Bird, J.P.: Space-charge limited conduction in epitaxial chromia films grown on elemental and oxide-based metallic substrates. AIP Adv. **9**, (2019). https://doi.org/10.1063/1.5087832
38. Chiu, F.C.: A Review on Conduction Mechanisms in Dielectric Films. Adv. Mater. Sci. Eng. (2014). https://doi.org/10.1155/204/58168
39. Zhou, H.F., Hou, Z.L., Kong, L.B., Jin, H.B., Cao, M.S., Qi, X.: Enhanced magnetization and improved leakage in Er-doped BiFeO3 nanoparticles. Phys. Status Solidi Appl. Mater. Sci. **210**, 809 (2013). https://doi.org/10.1002/pssa.201228693